PAPER • OPEN ACCESS

High-speed x-ray tomography of silo discharge

View the article online for updates and enhancements.

New Journal of Physics

The open access journal at the forefront of physics

CrossMark

PAPER

High-speed x-ray tomography of silo discharge

Ralf Stannarius[1] ⬤ , Diego Sancho Martinez[1], Tamás Börzsönyi[2], Martina Bieberle[3] ⬤ , Frank Barthel[3] and Uwe Hampel[3,4]

[1] Institute of Physics, Otto von Guericke University, D-39106 Magdeburg, Germany
[2] Institute for Solid State Physics and Optics, Wigner Research Centre for Physics, Hungarian Academy of Sciences, Budapest, Hungary
[3] Helmholtz-Zentrum Dresden—Rossendorf, Institute of Fluid Dynamics, Bautzner Landstr. 400, D-01328 Dresden, Germany
[4] Chair of Imaging Techniques in Energy and Process Engineering, Technical University Dresden, D-01062 Dresden, Germany

E-mail: ralf.stannarius@ovgu.de

Abstract

The outflow of granular materials from storage containers with narrow outlets is studied by means of ultrafast x-ray computed tomography (UFXCT). The used acquisition speed of this tomograph is high enough to allow high-speed recording of two horizontal cross sections (each of them at a rate of 1000 images per second) of the container during the discharge of material. Analyzing space-time plots that were generated from the tomograms, we retrieve velocity profiles and packing structures in the container. We compare hard spherical grains with soft, low-friction hydrogel spheres. Their flow profiles are qualitatively different. While the hard spheres form stagnant zones at the container side walls, the hydrogel spheres with extremely low friction coefficient flow in all regions of the container. Moreover, a shell-like positional arrangement of the soft spheres induced by the container walls is revealed. The results obtained for the flow field structure confirm earlier conclusions drawn from sequences of x-ray tomograms of clogged states.

1. Introduction

Granular material possesses a unique property: while it can be considered as solid when it is in a state of rest, the supply of external energy may cause a transition into a fluidized state where it can flow in a liquid-like manner. This feature has been exploited in technical devices for millennia. Hoppers are being widely used in agriculture to store grains, they can be filled by pouring material in from the top, and they are emptied conveniently on demand through an orifice at the bottom. Unlike the outflow of common liquids, the discharge of grains is qualitatively dependent on the size of the orifice. While liquids easily pass any orifices that are larger than their capillary length, a continuous outflow of grains requires a certain orifice diameter. For a large variety of hard, frictional spherical grains, it has been shown that the diameter of the opening must be larger than approximately five times the particle diameter to avoid clogs [1, 2]. When the particles are soft and slippery, they flow through much narrower outlets without clogging [3–5]. For non-spherical particles, shape parameters influence the discharge statistics [6, 7]. Despite the high practical importance of this process in agriculture, building industry, pharmacy and many other fields where grains are stored and processed, our understanding of the discharge of grains through narrow orifices is still quite incomplete.

The statistical characterization of the discharge of hard spheres from storage containers has been described in numerous papers in the past (e.g. [1, 2, 8–35]). Those studies dealt, e.g. with the determination of flow rates [1, 8–22], the statistics of clogging [2, 23–30], the influences of obstacles near the orifice on the flow rates [31, 32], and the role of gravity and embedding fluids [33–35]. The role of softness has been considered only recently in a few papers [3–5].

Silo discharge experiments in 2D containers with hydrogel spheres swollen in distilled water (9.2 mm diameter) have been reported before [4]. These experiments demonstrated qualitative differences of the discharge dynamics through narrow orifices as compared to rigid spheres. For 3D bins, similarly distinct flow profiles of the rigid spheres and hydrogel spheres were confirmed qualitatively by means of XR-CT [5]. One

peculiarity of the flow of hydrogel beads was that both in 2D and 3D containers, there were no stagnant zones. The complete content of the flat-bottomed bins participated in the outflow. The flow profile at sufficiently large distance from the bottom had plug-flow character [4].

While the statistics of the outflow can be determined with non-invasive methods very easily, for example by recording the mass of discharged grains as a function of time, the processes inside the hopper are largely concealed from the external observer. Theoretically, it would be possible to color-label grains during filling and to excavate the silo in clogged states, but this is an inefficient and cumbersome procedure. There are two possible approaches that can be used to access internal dynamic features: First, one may restrict to quasi-two dimensional (2D) containers with transparent front walls (e.g. [36–40]), where a direct optical observation is possible. However, it remains to be proven to what extent flow fields, clogged states and force chain networks observed in a 2D bin can be generalized to 3D containers. The second, more sophisticated technique is to employ non-invasive tools to determine the particle arrangements and dynamics in a 3D bin. X-ray computed tomography (XR-CT) [41, 42] or magnetic resonance imaging (MRI) [43] are the most promising candidates. Both methods have been successfully applied to map static granular ensembles. The problem with these 3D imaging tools is that they are very slow, compared to optical video imaging. Some elegant recent improvements allow to record fast particle motions with MRI (e.g. [44–46]). Contemporary technical equipment achieves temporal resolution of ≈ 7 ms. The usage of MRI requires liquid materials containing ^{1}H atoms, thus it is essentially restricted to the imaging of seeds, pharmaceutic pills, artificially designed small capsules or similar samples. An alternative is XR-CT, which can be used with a much broader range of materials. Conventional 3D XR-CT typically requires seconds to record single images, so it can only be applied to static granular ensembles, viz. clogged states of a silo [5, 6, 47], stepwise intrusion of a punch in a granular bed [48, 49], stepwise compression [50, 51] and others.
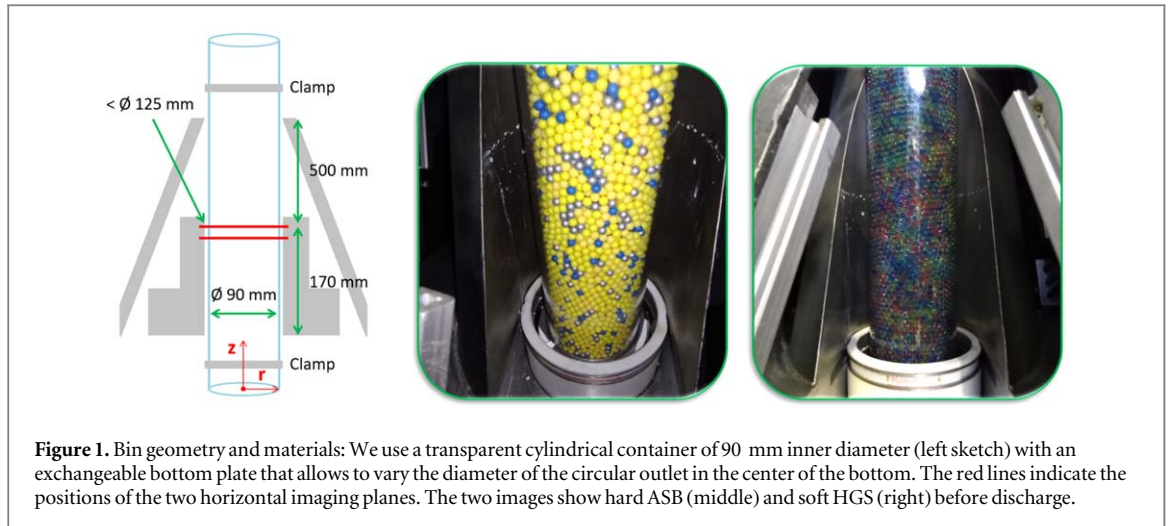
In order to visualize dynamic processes inside a container, one has to employ tricks. In silos, for example, one may create pulsating flow by opening the orifice only for short intervals. XR-CT images of silo discharge, for example, were recorded during the stopped phases with either the orifice closed [5] or in a clogged state [6]. Using image difference analysis one obtains local particle displacements as long as these are small enough for an unambiguous assignment of the grains. This method presupposes that the dynamics during avalanches are structurally equivalent to the flow profiles obtained from pulsed discharge, yet this hypothesis requires proof. Synchrotron x-ray tomography may provide sufficiently high beam intensity, but it has two drawbacks: conventional techniques are limited to approximately one tomogram per second or less, which is much too slow for the present task. Even with recent progress in sampling speeds for synchrotron microtomograms [52–54], the recording times of the order of hundred milliseconds per tomogram are insufficient for our purpose. More problematic, however, is the necessity of fast rotation of the sample during the measurement, which will disturb the discharge dynamics when the container size is of the order of centimeters. A rotation rate of 5 Hz, which is needed to obtain 10 tomograms per second, would generate centrifugal forces up to several *g* (gravitational acceleration).

The ultrafast x-ray computed tomography (UFXCT) at the Helmholtz-Zentrum Dresden-Rossendorf is a unique alternative. It allows to scan two planes in the container with sub-millisecond time resolution [55–57]. We use this technique to record the discharge of hard and soft grains from a cylindrical container, and we determine the essential features of the internal flow fields by image analysis. The results fully confirm our earlier hypothesis that the structure of the flow field during silo discharge is qualitatively different for the investigated hard, frictional and soft, low-friction spheres.

2. Experimental setup and materials

We compare two types of materials in this study. Airsoft bullets (ASB) are used as examples of rigid spheres. These particles are commercially available. They are monodisperse with diameters of 6 mm and consist of hard plastic. The ASB are hollow, but this aspect is not important for the present study.

Hydrogel spheres (HGS) are studied as examples of soft, low-friction grains. They have elastic moduli of the order of a few dozen kPa. The sliding friction coefficient on a glass plate has been determined to be approximately 0.02, one order of magnitude lower than that of the ASB. Similar hydrogels have been studied before [58–61]. In those experiments, the spheres were suspended in a fluorescence labeled fluid, and the characterization of static packings was in the focus of the investigations [60, 61]. The HGS used in our study are also monodisperse, but studied in air. Dry spheres were acquired from a commercial supplier (*Happy Store*, Nanjing). We swell them in salted water for at least 24 h before usage. The salt is used to control the final diameter of the swollen spheres. The salt concentration (NaCl) was chosen such that the diameter of the hydrogel spheres was also 6 mm, similar to the ASB. Before and after use, they were kept in the salt solution. Immediately before the experiments, the excess liquid at their surfaces was wiped off, and they were gravity-filled into the container.

Figure 1. Bin geometry and materials: We use a transparent cylindrical container of 90 mm inner diameter (left sketch) with an exchangeable bottom plate that allows to vary the diameter of the circular outlet in the center of the bottom. The red lines indicate the positions of the two horizontal imaging planes. The two images show hard ASB (middle) and soft HGS (right) before discharge.

The HGS slightly deform under the weight of overlying material in the silo, even in moderate depths of the granular bed. Their particle volume remains constant, the Poisson ratio is $1/2$.
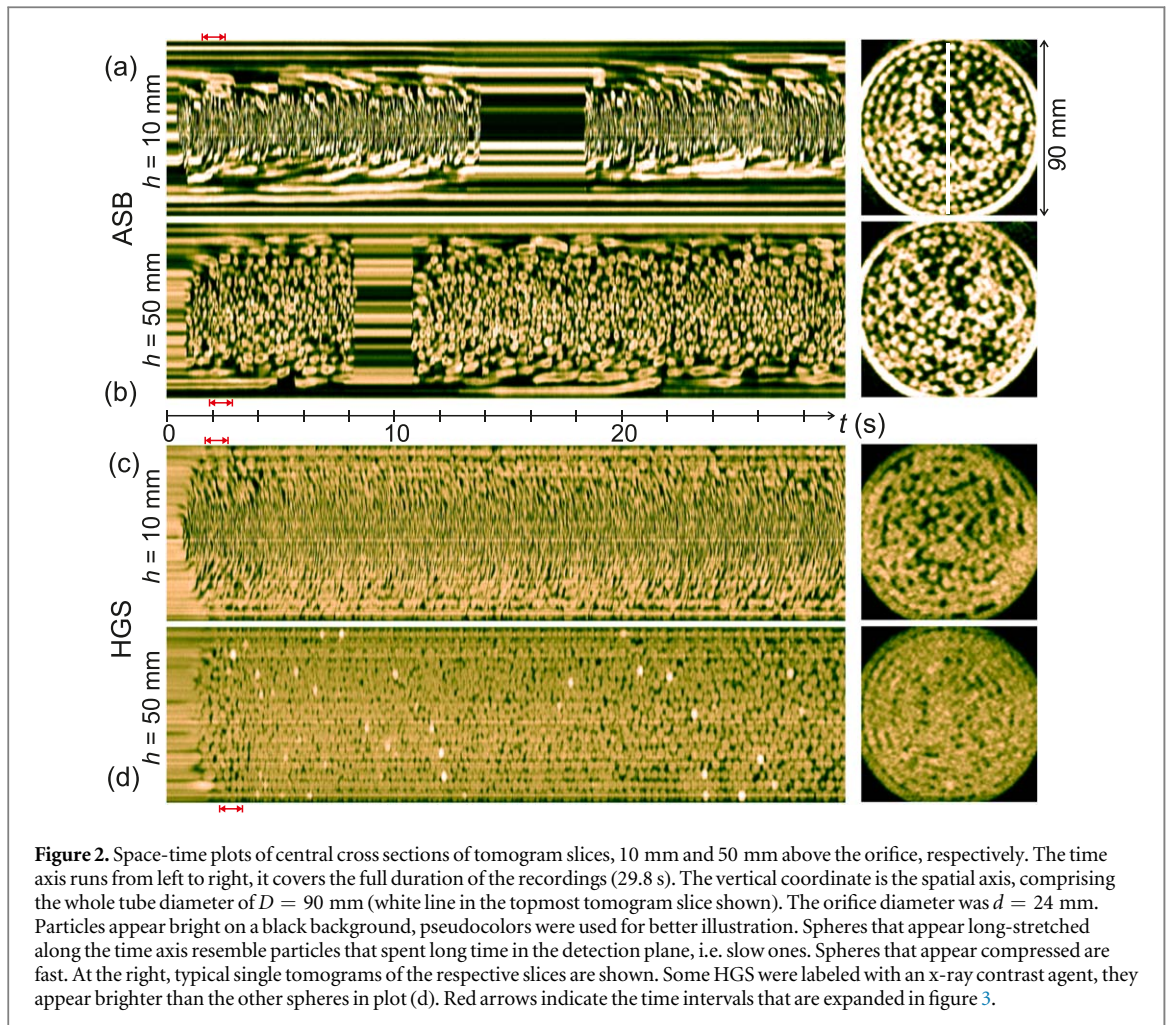
Some of the hydrogel spheres were labeled with an x-ray contrast agent (*Peritrast CT, Köhler-Chemie*) in order to increase their x-ray absorption. These particles can be identified individually in the images, for tracking purposes.

While the x-ray imaging experiments in the earlier 3D study [5] had to be performed on stationary states of the granular ensemble, the UFXCT equipment is sufficiently fast to record 1000 2D tomograms per second of each of two horizontal cross sections of the cylindrical container. This is achieved by deflecting an electron beam with a frequency of 2 kHz along a horseshoe shaped target encompassing the object of investigation. Where the electrons strike the target material, x-rays are generated. The radiation from this moving x-ray source spot penetrates the object and is measured by a static ring of fast x-ray detectors with a sampling rate of 1 MHz. As the two horizontal planes that are vertically separated by 11 mm from each other are recorded alternatingly, this results in 500 tomographic projections per beam revolution, from which cross sectional images are reconstructed using filtered backprojection. This allows live imaging of the granular flow as well as the measurement of axial velocities in the two detector planes. UFXCT has been demonstrated in several previous applications to provide real-time velocity data of granular ensembles [56, 57, 62–64]. A more detailed description of the UFXCT principle and the ROFEX (ROssendorf fast electron beam x-ray tomography) setup used here can be found in these publications. The maximum available temporal resolution is four times higher than the one chosen in our experiments. The tomograms consist of 256×256 pixels each, with pixel sizes of 0.47×0.47 mm². The thickness of the sensitive planes is approximately 2 mm.

The experiments were performed as follows: The material was loaded to a cylindrical container with 80 cm height and inner diameter of $D = 90$ mm (figure 1), with the outlet closed by a lid. Then, recording of the XR-CT sequences was started and simultaneously, the lid was opened by remote control. We recorded sequences of approximately 30 s duration. This yields two sequences of about 29 800 images for each run, corresponding to the two detector planes. The diameter $d = 24$ mm of the circular orifice in the bottom of the tube was chosen such that the material either did not clog at all, or at least provided large enough avalanches of 15 s or longer duration on average. The container did never run empty during the recording, at least 20 cm fill height remained in the silo at the end of each run. In some experiments with the hard ASB, the system produced clogs. In those cases, flow was restarted by a manually triggered airflush into the orifice [7].

We selected different heights of the sensitive planes, by appropriately adjusting the position of the container before the recording. In a first set of experiments, the position of the lower plane was chosen 10 mm above the container bottom (the second plane 21 mm above the bottom). Then, we moved the silo tube down for following experiments such that the planes were at heights 30 and 41 mm above the bottom, then 50 and 61 mm above the bottom and so on. Assuming that the flow speed and profile statistics is the same for all individual discharge events, it is possible in principle to collect flow speeds in arbitrary heights of the container and to assemble representative flow profiles for a given material and outlet size.

For each parameter set, up to three individual discharge experiments were performed. These runs gave statistically equivalent results, except that in some experiments with the hard grains, clogs formed spontaneously. In those cases, we evaluated only the tomograms recorded before and after the clog.

Figure 2. Space-time plots of central cross sections of tomogram slices, 10 mm and 50 mm above the orifice, respectively. The time axis runs from left to right, it covers the full duration of the recordings (29.8 s). The vertical coordinate is the spatial axis, comprising the whole tube diameter of $D = 90$ mm (white line in the topmost tomogram slice shown). The orifice diameter was $d = 24$ mm. Particles appear bright on a black background, pseudocolors were used for better illustration. Spheres that appear long-stretched along the time axis resemble particles that spent long time in the detection plane, i.e. slow ones. Spheres that appear compressed are fast. At the right, typical single tomograms of the respective slices are shown. Some HGS were labeled with an x-ray contrast agent, they appear brighter than the other spheres in plot (d). Red arrows indicate the time intervals that are expanded in figure 3.

3. Qualitative data analysis

Different approaches were used to extract the desired information on packing structure and velocity from the tomogram sets. The simplest analyzes are space-time plots of central cross sections of the recorded tomograms. Due to the symmetry of the setup, all cross sections with different azimuth angles (in the polar coordinate system aligned with the tube axis) are equivalent. Therefore it is sufficient here for demonstration purposes to show representative cross section plots for each material, each compiled from 29 800 2D frames recorded at 1000 fps. Such plots are shown in figures 2 and 3. Figure 2 contains plots of an arbitrarily chosen central line of the set of tomogram slices (vertical in the single slices at the right). For an overview, we have chosen two tomogram sequences of the lower detector plane, recorded 10 mm and 50 mm above the orifice level, respectively, for each type of material. These spatio-temporal plots allow a comprehensive qualitative characterization of the internal flow fields. More details are seen in zoomed views of a representative 1 s period, starting 5 s after the initiation of the flow (figure 3). The space-time plots can be interpreted as follows:

ASB, figures 2, 3(a): The outflow started when the outlet was opened, 0.5 s after the begin of the record. The flow clogged spontaneously after 13.8 s. It was restarted manually by an air flush at time 18.4 s. During the avalanches, we did not find any noticeable qualitative changes of the pattern in time, except when the clog stopped the outflow. The continuous lines near the container wall (top and bottom of the plot 2(a)) represent immobile grains in the stagnant zone. The particle images appear shorter the closer they are to the center, i.e. the velocity continuously increases towards the inner core of the silo. One can also estimate from the plots that the vertical velocity component is practically time-independent, i.e. the flow is stationary. In addition to the vertical motion (which stretches the images along the time axis), a slight radial inward motion is evident, particularly in the shear zone between the stagnant part and the flowing core material. The particle images in that region have a slight inclination towards the center in the space-time plots. There is no radially outward flow of grains.

ASB, figures 2, 3(b): The second space-time plot of hard grains was recorded at a height of 50 mm. The outflow was triggered 0.8 s after start of the recording, it clogged at time 8.2 s and was restarted again at time 10.8 s. There are still some stagnant zones near the walls, reflected in horizontal uninterrupted lines, but in some
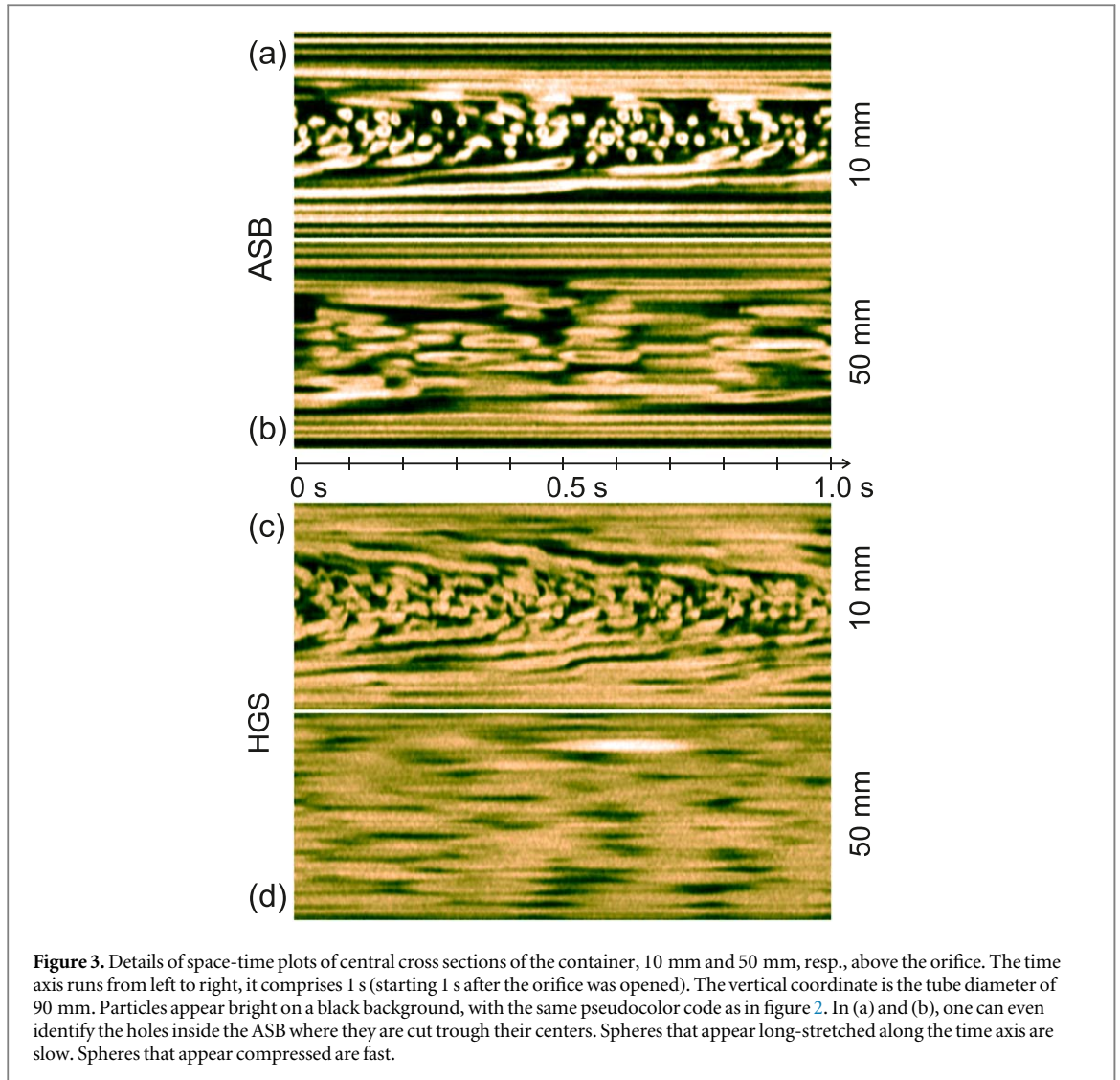
Figure 3. Details of space-time plots of central cross sections of the container, 10 mm and 50 mm, resp., above the orifice. The time axis runs from left to right, it comprises 1 s (starting 1 s after the orifice was opened). The vertical coordinate is the tube diameter of 90 mm. Particles appear bright on a black background, with the same pseudocolor code as in figure 2. In (a) and (b), one can even identify the holes inside the ASB where they are cut trough their centers. Spheres that appear long-stretched along the time axis are slow. Spheres that appear compressed are fast.

places (bottom of the space-time plot), the flowing zone reaches the wall. The velocity increases towards the core in a narrow shear zone. In a core region of about 40 mm diameter, the flow velocity is nearly uniform. The flow is almost completely vertical, the particle images are extended almost exactly in the direction of the time axis (figure 3(b)). The comparison of the zoomed views in figures 3(a), (b) also shows that the velocity in the flowing zone is much smaller in the upper slice. This is the consequence of the wider diameter of the flowing zone at 50 mm height, in combination with mass conservation in this stationary flow. Far from the bottom, hardly more than one layer of spheres remains immobile at the container wall. A shear band approximately two particle diameters thick separates this layer from the rest of the material in the tube center, which flows with nearly uniform speed.

An interesting detail of the flow profile in all slices is the transient behavior after the start of the first discharge. The flowing zone slightly widens at the beginning of the *first* avalanche. When the discharge is started, the flowing region in 10 mm height above the bottom (figure 2(a)) starts with a diameter of about 45 mm and it expands within one second to the full width of ≈65 mm. When the flow is restarted after the clog, the material remembers this last value and restarts with the full width. The same is seen in the 50 mm slice (figure 2(b)): The first avalanche after filling the silo starts with a floating region roughly 43 mm wide, and it expands to about 75 mm within about two seconds. The second avalanche triggered in the clogged state starts with full width from the beginning. This indicates that some structural reorganization is going on after the onset of the flow, which we will discuss in more detail below.

HGS, figures 2, 3(c): The spatial structure of the flow field is completely different for the soft, low-friction spheres. It is seen in both figures that *all* particles in the bottom part of the silo participate in the flow. The discharge starts in a narrow central region with a diameter comparable to the orifice, and it expands during approximately 1.2 s to the whole tube cross section. Even the grains directly at the walls move downward, albeit with lower speed than those in the tube center (figure 3(c)). There is a clear inward radial motion of all grains
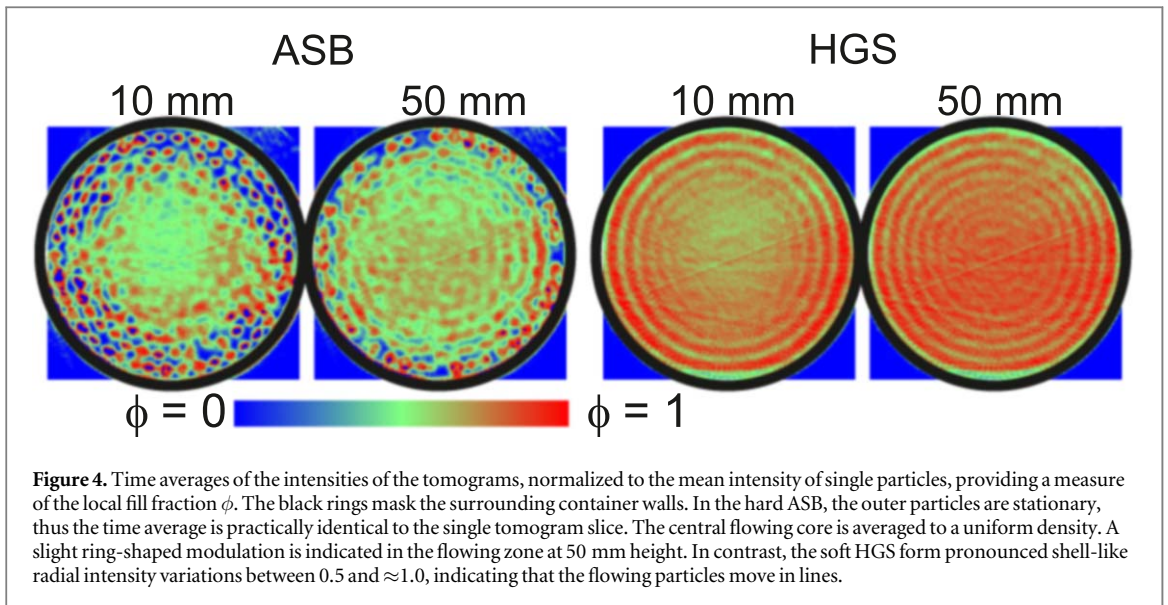
Figure 4. Time averages of the intensities of the tomograms, normalized to the mean intensity of single particles, providing a measure of the local fill fraction ϕ. The black rings mask the surrounding container walls. In the hard ASB, the outer particles are stationary, thus the time average is practically identical to the single tomogram slice. The central flowing core is averaged to a uniform density. A slight ring-shaped modulation is indicated in the flowing zone at 50 mm height. In contrast, the soft HGS form pronounced shell-like radial intensity variations between 0.5 and ≈ 1.0, indicating that the flowing particles move in lines.

near the bottom except near the center, directly above the orifice. The velocity of the central particles is roughly comparable to that of the hard spheres. The conclusion is that discharge rates do not crucially depend on softness and friction. This confirms, at least approximately, the predictions of Beverloo's equation [9] which establishes a relation between the orifice and particle diameters, disregarding softness and friction.

HGS, figures 2, 3(d): The scans in 50 mm height above the orifice confirm that there is no stagnant region for the soft grains, but there is an additional new feature: the vertical velocities level out in the silo cross section. Grains in the central part are slower, and grains in the outer parts become faster than in the bottom slice. The flow becomes plug-like, there is practically no radial gradient in the vertical velocity anymore. There is also no measurable radial component of the flow field in this distance from the outlet (see figure 3(d)).

One immediately evident feature of the discharge of HGS is that the flow is slightly time-dependent. In figures 2(c), (d), the extensions of the particle images along the time axis increase with progressing time, i.e. the vertical velocity decays in the course of the discharge. This is a typical feature of the soft HGS, which is probably related to the lowering pressure at the silo bottom with decreasing fill height. The flow speed decreases while the pressure at the orifice drops. Thus, the above statement regarding Beverloo's equation holds only approximately for the HGS. Pressure plays a non-negligible role in the discharge rate of soft, low-friction particles. It remains to be clarified whether the softness, the low friction or a combination of both is responsible for this feature.

Another astonishing feature is the spatial arrangement of the HGS particles in some shell-like positional ordering by the flow. This is indicated already in figure 2(d). The soft spheres follow typtical 'lanes'. Such behavior is not found for the hard particles. It can be visualized best when one computes the temporal average over all tomogram slices recorded after the start of discharge (excluding the clogged states). Figure 4 shows the results of the four selected experiments. For the ASB, the intensity profile in the outer, stagnant zones reflects only the accidental static distribution of the immobile outer grains. In the central, flowing zone, the average yields a more or less uniform intensity corresponding to a packing fraction $\phi \approx 0.6$, slightly smaller than that of random close sphere packing. In contrast, the soft HGS flow everywhere and a preferential shell-like order is seen in all tomographic slices. At the height of 10 mm, the average packing fraction is noticeably lower than in the higher slices. This is a consequence of the larger velocities. At higher elevation, one finds plug flow, no shear or other grain rearrangements. Near the outlet (at $h = 10$ mm) however, the system is subject to radial shear gradients, which leads to a lower packing fraction. In radial direction, 8–9 shells are formed, i.e. the positional order induced by the outer silo walls penetrates the complete container. The width of each of these shells is slightly smaller than one particle diameter.

A reasonable relation between the averaged intensities and the local mean packing fraction ϕ of the grains was established with the following procedure: we divided the intensity of a given pixel averaged over the complete set of tomograms in one run of the experiment by the mean intensity of particles in a single tomogram. This should be equal to the probability that the pixel is occupied by a particle, and likewise to the ratio $\phi = V_p/V_0$ of the mean volume occupied by particles, V_p, and the total volume V_0. The absolute uncertainty of the local packing fraction ϕ obtained with this method may be of the order of 10%, but the relative error is lower. A good benchmark for the accuracy of calibration is the intensity of pixels in the container wall.

4. Quantitative data evaluation

While the qualitative analysis of the tomogram sequences already provides all essential features of the flow field inside the containers, it is highly desirable to achieve a *quantitative* picture of the grain dynamics. For that purpose, several approaches are possible. First, one can determine the exact passage times of individual particles through the slices. However, this method is rather inaccurate, particularly because of the noise in the tomograms. Second, one may trace labeled grains passing the upper plane first and then the lower plane. This method samples the velocity field, and it provides all three components, vertical, radial and tangential. One may also measure temporal correlations between the simultaneously recorded tomograms of the upper and lower planes. From the time delay between spatial patterns in both planes, the vertical velocity can be determined statistically (a variant of particle image velocimetry). The method we use here is simpler, it exploits the statistics of the temporal intensity fluctuations in each slice. Its advantage over the latter two methods is that the spatial accuracy is much higher, since it measures the vertical velocity component at the position of the tomogram slices. Since this method is indirect, one may have to calibrate it with tracer data.

The principle is as follows: we assume that the spheres are randomly distributed in the container during the discharge. This is a rough approximation for HGS where we disregard for the moment the shell-like ordering. The relevance of this detail will be discussed later. In a container with randomly packed immobile spheres, one can determine the average *spatial* autocorrelation function (ACF) $\mathcal{G}_s(\Delta s)$ in any given direction $s = \{x, y, z\}$. When this container is moved along z with a constant velocity v_z, then one obtains a *temporal* ACF $\mathcal{G}_t(\Delta t) \equiv \mathcal{G}_s(v_z \Delta t)$ at any given spatial position. Assuming in first approximation that the silo outflow is stationary and thus that grains passing a given pixel of the (x, y) tomogram slice have the same average velocity $v_z(x, y)$, one can compare the temporal autocorrelation function $\mathcal{G}_t(\Delta t) = \mathcal{G}_s(v_z \Delta t)$ in each point of the tomogram with $\mathcal{G}_s(\Delta z)$ obtained from a container filled with the same grain types at rest. Then, v_z is found by fitting. The faster the vertical velocity component v_z, the shorter is the decay of the temporal ACF. For a quantitative evaluation, all that is needed is $\mathcal{G}_s(\Delta s)$.
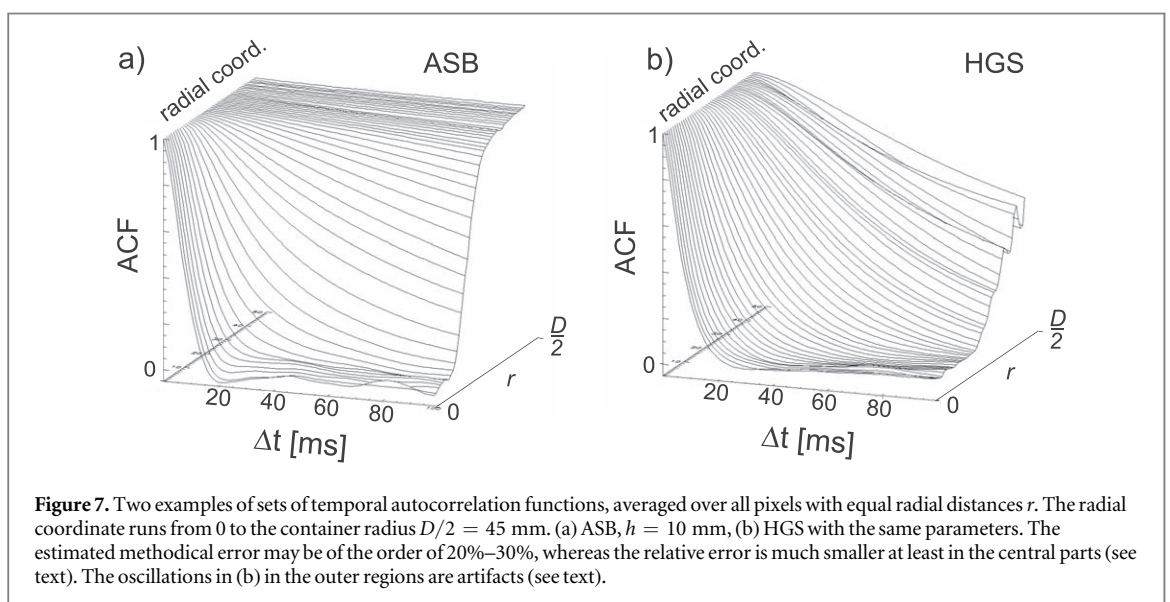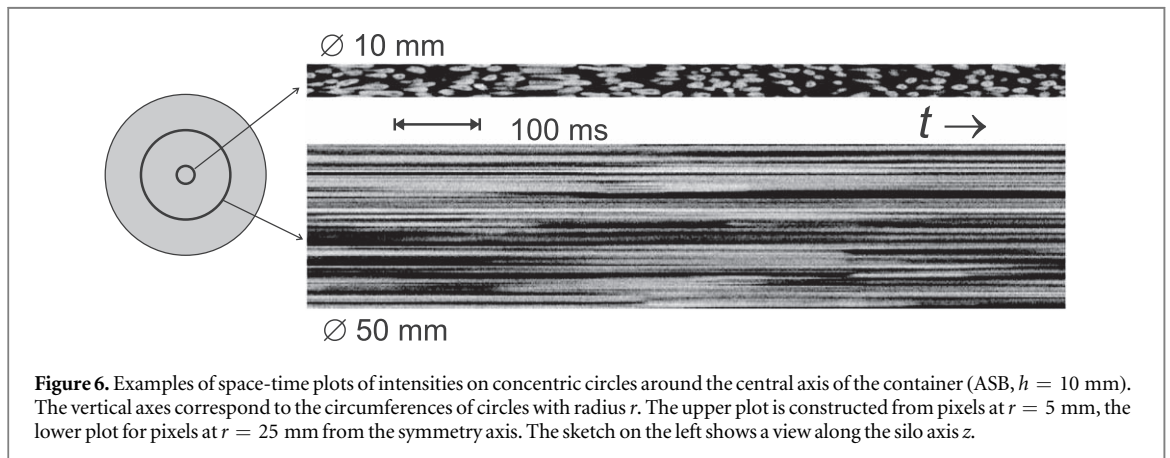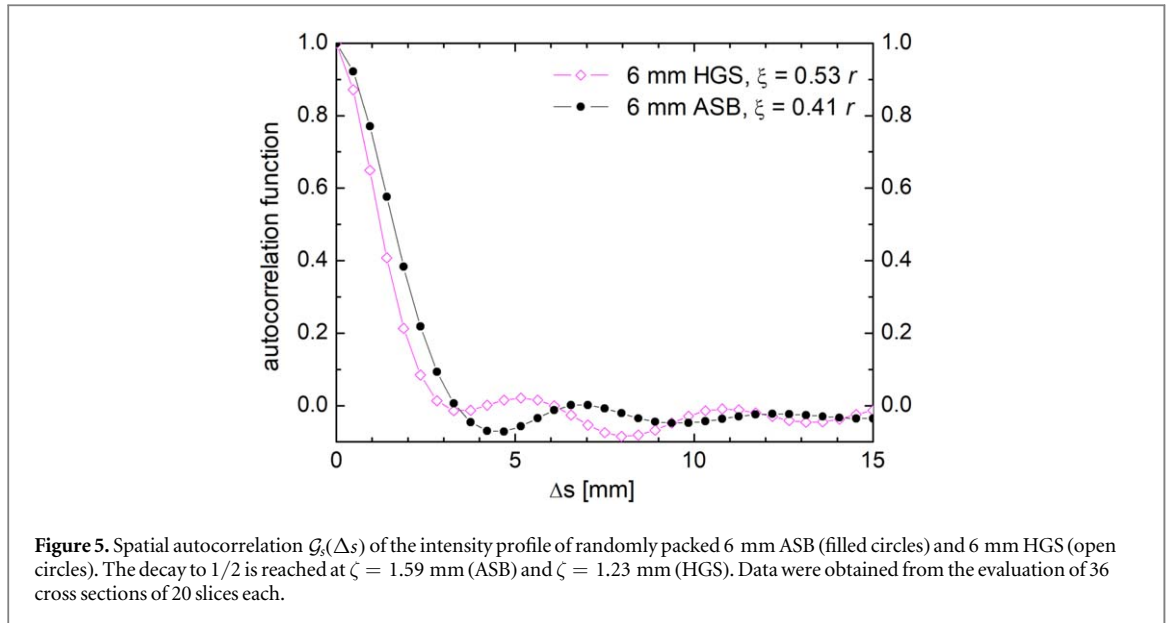
Assuming spatial isotropy in the container, the spatial autocorrelation function $\mathcal{G}_s$ is equivalent for all coordinates x, y, z. It can, in principle, be calculated for randomly packed spheres. An experimental access to $\mathcal{G}_s$ is to analyze x-ray tomograms measured in a static random packing. One can use, for example, data obtained with a 3D tomograph (e.g. with the Siemens Artis zeego x-ray tomograph at Otto von Guericke University, Magdeburg used in previous studies of similar samples [5]). Here, we decided to retrieve the spatial autocorrelation functions directly from the UFXCT tomograms, even though the latter have a higher noise level. This has the advantage that influences of differences in the instrument response functions or in the signal-to-noise ratios are eliminated. For that purpose, we analyze a large number of tomograms, and determine the spatial autocorrelation functions for randomly selected cross sections. These are averaged to obtain a good approximation for $\mathcal{G}_s(\Delta s)$.

One finds typical decays from $\mathcal{G}_s(0) = 1$ to $\mathcal{G}_s(\Delta s \rightarrow \infty) = 0$, superimposed by weak oscillations of a wavelength comparable to the particle diameter. The results are shown in figure 5. The autocorrelations decay to $1/2$ within characteristic correlation lengths of $\zeta = 1.59$ mm (ASB) and $\zeta = 1.23$ mm (HGS). The slightly better spatial correlations in the ASB tomograms may be the consequence of the higher signal-to-noise ratio for this material. Because both values are much smaller than the particle diameters, we suppose that influences of details of the random packing, and in particular of the fill fractions (in the typical range for close-packed spheres), are not critical for the shape of the initial characteristics of $\mathcal{G}_s$. Correlations over distances larger than the particle diameters are not expected to influence the initial decay dramatically. This justifies our method as a reasonable approximation even for packings that are not completely random.
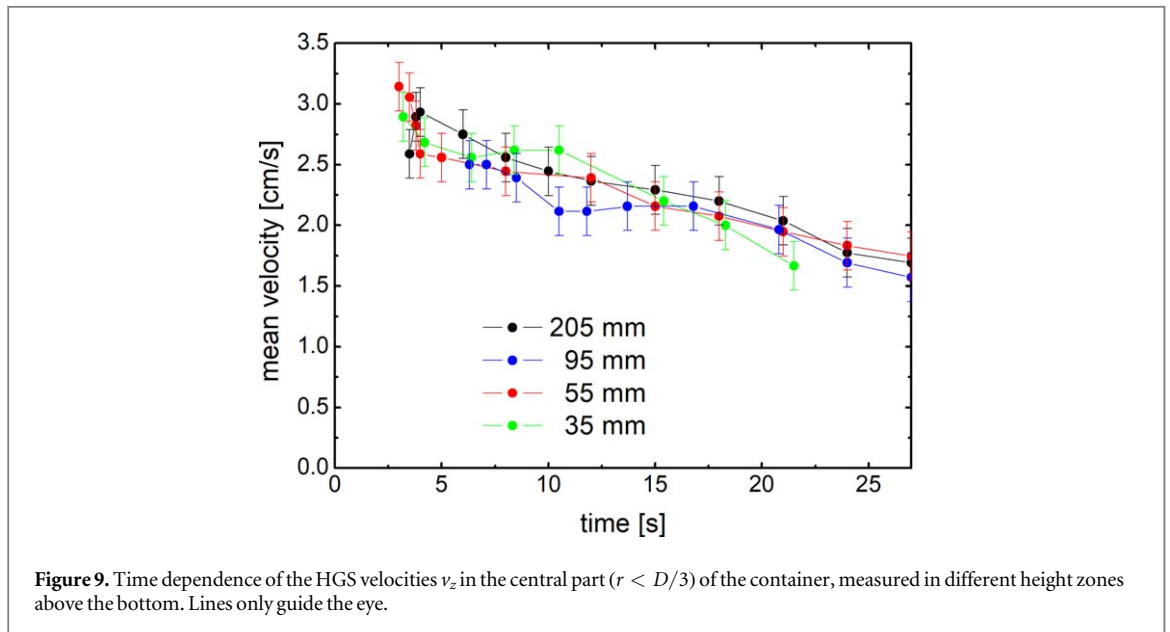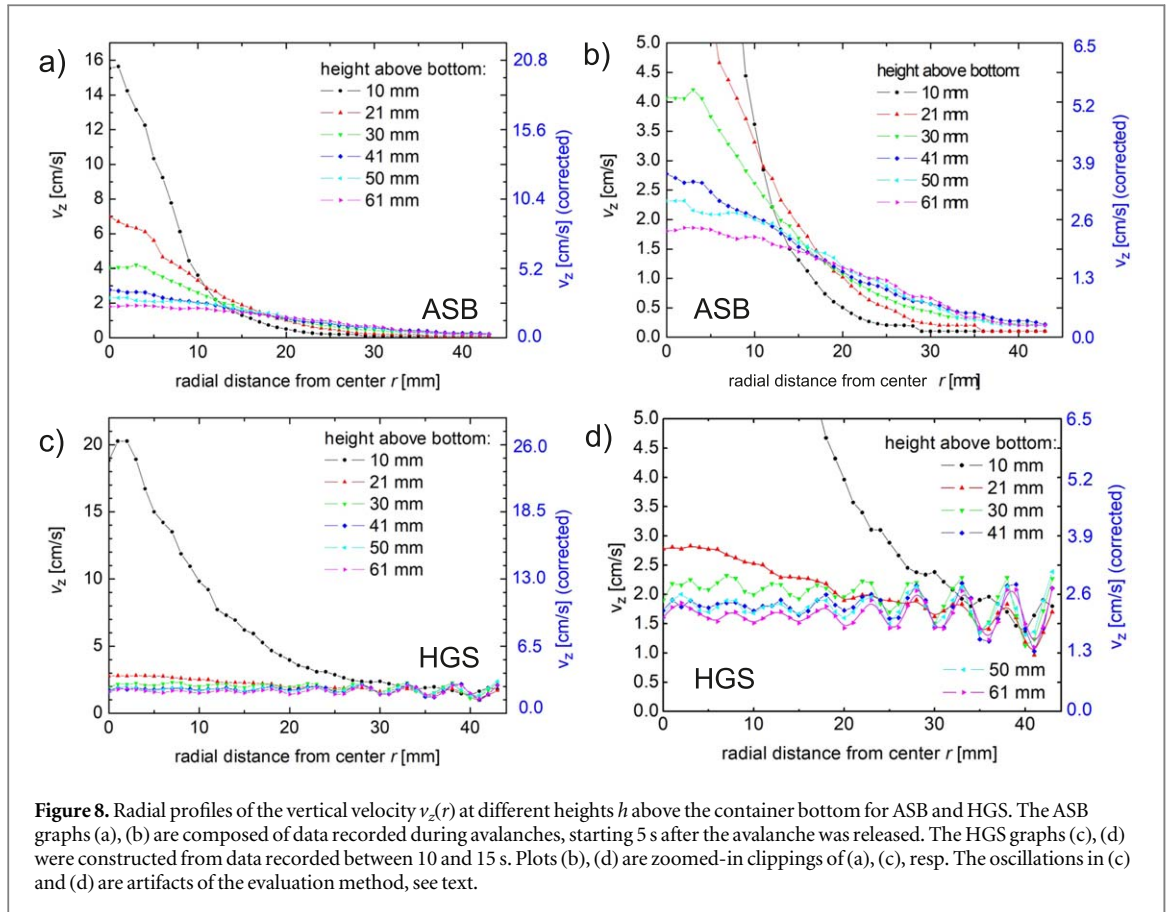
For the determination of the mean temporal ACFs, we assume that all particles in a given distance r from the central axis of the container have the same mean velocity. Examples of space-time plots of pixels with equal distances r for ASB in a height $h = 10$ mm above the bottom are shown in figure 6. For fixed r, we calculate the temporal ACFs of each pixel and take the average. These functions are compared to the respective $\mathcal{G}_s(\Delta s)$ from the static tomograms (figure 5), and $v_z(r)$ is obtained by fitting.

Figure 7 exemplarily shows two sets of temporal ACFs, averaged over all pixels with equal radial distances r. They were computed for the $h = 10$ mm slice. It is seen that the autocorrelation functions ASB (figure 8(a)) decay rapidly only in the center of the silo, for $r < 20$ mm. At the container boundaries, the decay is very slow, which evidences that there is practically no particle motion. For the HGS at the same height level, a noticeable decay is found for all radii, which means that the HGS spheres move vertically everywhere.

Figure 8 shows the vertical velocities v_z at different heights, determined from the uncorrected fits to the spatial ACFs. A systematic correction (right axes) is described below. For the ASB, the function $v_z(r)$ decays at all height levels much more rapidly towards the outer walls than for HGS. For the latter, the vertical velocity is close to 20 mm s^{-1} even near the walls, whereas it drops below the experimental resolution for the hard ASB. This is in accordance with the qualitative conclusions derived from the space-time plots, and it is also in good agreement

Figure 5. Spatial autocorrelation $\mathcal{G}_s(\Delta s)$ of the intensity profile of randomly packed 6 mm ASB (filled circles) and 6 mm HGS (open circles). The decay to $1/2$ is reached at $\zeta = 1.59$ mm (ASB) and $\zeta = 1.23$ mm (HGS). Data were obtained from the evaluation of 36 cross sections of 20 slices each.

Figure 6. Examples of space-time plots of intensities on concentric circles around the central axis of the container (ASB, $h = 10$ mm). The vertical axes correspond to the circumferences of circles with radius r. The upper plot is constructed from pixels at $r = 5$ mm, the lower plot for pixels at $r = 25$ mm from the symmetry axis. The sketch on the left shows a view along the silo axis z.

Figure 7. Two examples of sets of temporal autocorrelation functions, averaged over all pixels with equal radial distances r. The radial coordinate runs from 0 to the container radius $D/2 = 45$ mm. (a) ASB, $h = 10$ mm, (b) HGS with the same parameters. The estimated methodical error may be of the order of 20%–30%, whereas the relative error is much smaller at least in the central parts (see text). The oscillations in (b) in the outer regions are artifacts (see text).

with earlier predictions from pulsed discharge [5]. Note that the outflow velocity of HGS is slightly time-dependent (see figure 9 below). This is already seen in figure 2(d). The values shown in figure 8 were constructed from data taken roughly in the middle of the discharge. More details of the ξ time dependence are discussed below.

Figure 8. Radial profiles of the vertical velocity $v_z(r)$ at different heights h above the container bottom for ASB and HGS. The ASB graphs (a), (b) are composed of data recorded during avalanches, starting 5 s after the avalanche was released. The HGS graphs (c), (d) were constructed from data recorded between 10 and 15 s. Plots (b), (d) are zoomed-in clippings of (a), (c), resp. The oscillations in (c) and (d) are artifacts of the evaluation method, see text.

Figure 9. Time dependence of the HGS velocities v_z in the central part ($r < D/3$) of the container, measured in different height zones above the bottom. Lines only guide the eye.

The oscillations that appear in the velocity profile of the HGS in the outer region are artifacts of the evaluation method. The procedure assumes that the packing density of flowing grains is comparable to that of the particles at rest, which is not correct in the outer regions with strong layering (figure 4). In that region, the spheres form lanes, and the method overestimates or underestimates the velocities obtained from temporal ACFs, depending on where the ACF is taken. One can expect accurate velocity data only for the spatial average across a 'lane'. Then, the results for levels above 30 mm height are consistent with a plug flow behavior, which is certainly the consequence of the low friction at the smooth container walls. At higher levels, there is no noticeable dependence of v_z on height or radial position. The potential reason is the very low friction of the HGS

at the container walls. In contrast, we find a radial shear gradient of $v_z(r)$ at all levels for the ASB. This gradient gradually decreases with increasing height level.

The ACF method makes some assumptions that may lead to systematic errors. In some experiments with HGS where we used labeled tracer spheres (see figures 2(d) and 3(d)), it is possible to test the accuracy of the ACF evaluation method and to calibrate the computed vertical velocities. For that purpose, we determined the time intervals from the moment a labeled sphere enters the upper detector slice to the moment when it becomes visible in the lower slice. Dividing the distance between the two tomogram planes by the time delay, one obtains the vertical velocity v_z directly, with a much higher precision (5 … 10%) than from the ACFs. This velocity is an average over the distance between the two slices. With the tracer method it is even possible to obtain a radial profile of v_z. Yet as we had already established, there is practically no radial dependence of v_z for the HGS. Thus it is sufficient to present the mean values $\overline{v_z}(t)$ (spatial average) in figure 9. The height levels given in the plot denote the middle of the zone between the two detection planes, rounded to mm. For example, '205 mm' marks the passage from 211 mm height down to 200 mm. At the container bottom (between the 10 and 21 mm planes), the tracer velocities are not uniform, thus we have excluded these planes in the plot.

Two features are immediately evident from these plots:

(1) There is no noticeable height level dependence of the mean vertical velocities $\overline{v_z}(t)$ of HGS, in accordance with the autocorrelation data of figure 8.

(2) The vertical velocities decrease with decreasing fill height of the container. For the first data points obtained with the tracer method, after about 3.5 s, the remaining fill height is slightly more than 70 cm, and $\overline{v_z}(t)$ is between 27 and 30 mm s^{-1}. Near the end of the experiment, after 27 s, the remaining fill height is about 25 cm, and $\overline{v_z}(t)$ has dropped to $\approx$17 mm s^{-1}.

The values found with the autocorrelation method deviate by about 30% from the more direct tracer method. This underestimation of the actual velocities has to be attributed to the more complex and indirect data analysis of the former approach. The main error source is probably the thickness of the sensitive slice. The resolution in z direction (sensitive slice thickness) is 2 mm in contrast to the 0.47 mm pixel size within the plane, thus the particles need more time to pass the slice than expected for a cubic voxel. Consequently, the ACF approach overestimates the mean residence time in the measurement plane and the autocorrelation functions drop correspondingly slower than they would do for a thin detection slice. The error is systematic and it leads to an underestimation of the particle velocities roughly by up to 30%. One may use this estimate to correct the velocities determined from ACFs (right axis in figure 8), and arrive at absolute velocities that are comparable with the tracer results. In any case, the ACF evaluations provide valuable spatially resolved information and the relative accuracy is uninfluenced by this correction. We assume that the same rescaling is appropriate for the ASB, which have similar sizes.

5. Summary

Ultrafast x-ray Computed Tomography has been employed to characterize flow profiles inside containers with small orifices. Horizontal slices of the container were imaged with a speed of 1000 frames/s. It has been demonstrated that the temporal resolution of the method is sufficient to identify individual particles in the container during their passage through the sensitive slices. Not only does the experiment provide an easy access to the structure and qualitative features of the velocity fields, but it can also be used to obtain quantitative information. The method has been applied to study monodisperse ensembles of spherical particles, one type with rigid shape, the second one with very low friction and additional shape-elasticity. Their outflow characteristics are qualitatively different. The hard ASB form stagnant regions of immobile spheres at the container walls, even in appreciable distance from the outlet. The elastic HGS flow in the complete container, at some height above the outlet (of the order of the container radius), the flow field becomes uniform and independent of the radial distance from the walls, even the material directly at the walls slides down with a velocity comparable to that of the inner regions. Thereby, the soft HGS develop a distinct structural layering. Positional ordering induced by the outer walls penetrates the cylindrical container with an appreciable correlation length. In the containers used here, with a diameter of approximately 15 particles, the induced shell-like order penetrates the complete tube.

The flow rate of the hard ASB is independent of the fill level of the bin, at least in the height range of our experiment, down to a height of the granular bed of about 2 tube diameters. In contrast, the flow velocity of the soft HGS decreases noticeably with progressing discharge of the container. This is in accordance with earlier qualitative observations in 2D containers [4], where it was found that the pressure near the outlet is nearly hydrostatic for HGS, and lower pressure leads to a reduced outflow rate.

The experimental technique used here has the potential to obtain detailed information on dynamic processes of granular ensembles in containers with small orifices. Among the unresolved problems are, for example, structures of stagnant zones in containers with non-circular cross sections, the effect of obstacles near orifices on the flow, and the structure of flow fields in containers with other than cylindrical shapes, e.g. conical hoppers. Moreover, the technique opens the opportunity to study in detail the influence of particle shapes (e.g. rods, flattened lentils, irregularly shaped beads, complex particles that can entangle). While x-ray contrast agents may be helpful to increase contrast and to label single particles as tracers, the present study shows that essential information can be obtained without this, so that the method has the potential to be used with a broad class of granular materials from construction industry, agriculture, pharmacy, and many other fields.

Acknowledgments

ORCID iDs

Ralf Stannarius ⓘ https://orcid.org/0000-0002-6836-3663
Martina Bieberle ⓘ https://orcid.org/0000-0003-2195-6012

References

[1] Zuriguel I, Garcimartín A, Maza D, Pugnaloni L A and Pastor J M 2005 *Phys. Rev. E* **71** 051303
[2] Thomas C C and Durian D J 2015 *Phys. Rev. Lett.* **114** 178001
[3] Hong X, Kohne M, Morrell M, Wang H R and Weeks E R 2017 *Phys. Rev. E* **96** 062605
[4] Ashour A, Trittel T, Börzsönyi T and Stannarius R 2017 *Phys. Rev. Fluids* **2** 123302
[5] Stannarius R, Martinez D S, Finger T, Somfai E and Börzsönyi T 2019 *Granular Matter* **21** 56
[6] Börzsönyi T, Somfai E, Szabó B, Wegner S, Mier P, Rose G and Stannarius R 2016 *New J. Phys.* **18** 093017
[7] Ashour A, Wegner S, Trittel T, Börzsönyi T and Stannarius R 2017 *Soft Matter* **13** 402
[8] Franklin F C and Johanson L N 1955 *Chem. Eng. Sci.* **4** 119–29
[9] Beverloo W A, Leniger H A and Van de Velde J J 1961 *Chem. Eng. Sci.* **15** 260
[10] Neddermann R M, U Tuzun, Savage S B and Houlsby G T 1982 *Chem. Eng. Sci.* **37** 1597–609
[11] Chang C S, Converse H H and Steele J L 1991 *Trans. Am. Soc. Agric. Eng.* **34** 1789–96
[12] To K 2005 *Phys. Rev. E* **71** 060301
[13] Mankoc C, Janda A, Arévalo R, Pastor J M, Zuriguel I, Garcimartín A and Maza D 2007 *Granular Matter* **9** 407–14
[14] Hilton J E and Cleary P W 2011 *Phys. Rev. E* **84** 011307
[15] Garcimartín A, Zuriguel I, Janda A and Maza D 2011 *Phys. Rev. E* **84** 031309
[16] Uñac R O, Vidales A M, Benegas O A and Ippolito I 2012 *Powder Technol.* **225** 214–20
[17] Masuda T, Nishinari K and Schadschneider A 2014 *Phys. Rev. Lett.* **112** 138701
[18] Benyamine M, Djermane M, Dalloz-Dubrujeaud B and Aussillous P 2014 *Phys. Rev. E* **90** 032201
[19] Janda A, Harich R, Zuriguel I, Maza D, Cixous P and Garcimartin A 2009 *Phys. Rev. E* **79** 031302
[20] Sheldon H G and Durian D J 2010 *Granular Matter* **12** 579–85
[21] Saraf S and Franklin S V 2011 *Phys. Rev. E* **83** 030301
[22] Zuriguel I, Maza D, Janda A, Hidalgo R C and Garcimartín A 2019 *Granular Matter* **21** 47
[23] To K, Lai P Y and Pak H K 2001 *Phys. Rev. Lett.* **86** 71
[24] Manna S S and Herrmann H J 2000 *Eur. Phys. J. E* **1** 341–4
[25] Zuriguel I, Pugnaloni L A, Garcimartín A and Maza D 2003 *Phys. Rev. E* **68** 030301
[26] Janda A, Zuriguel I, Garcimartín A, Pugnaloni L A and Maza D 2008 *Europhys. Lett.* **84** 44002
[27] Zuriguel I 2014 *Pap. Phys.* **6** 060014
[28] Zuriguel I *et al* 2014 *Sci. Rep.* **4** 7324
[29] Thomas C C and Durian D J 2013 *Phys. Rev. E* **87** 052201
[30] Tang J and Behringer R P 2011 *Chaos* **21** 041107
[31] Zuriguel I, Janda A, Garcimartín A, Lozano C, Arévalo R and Maza D 2011 *Phys. Rev. Lett.* **107** 278001
[32] Lozano C, Janda A, Garcimartín A, Maza D and Zuriguel I 2012 *Phys. Rev. E* **86** 031306
[33] Dorbolo S *et al* 2013 *Granular Matter* **15** 263–73
[34] Arévalo R and Zuriguel I 2016 *Soft Matter* **12** 123
[35] Wilson T J, Pfeifer C R, Meysingier N and Durian D J 2014 *Pap. Phys.* **6** 060009
[36] To K 2002 *Chin. J. Phys.* **40** 379
[37] Tang J and Behringer R P 2016 *Europhys. Lett.* **114** 34002
[38] Maiti R, Das G and Das P K 2017 *Phys. Fluids* **29** 103303
[39] Gella D, Maza D and Zuriguel I 2017 *Phys. Rev. E* **95** 052904
[40] Zhong C, Guo X, Xu J, Li W, Lu H and Liu H 2019 *Powder Technol.* **343** 237–44
[41] Weis S and Schröter M 2017 *Rev. Sci. Instrum.* **88** 051809
[42] Maire E and Withers P J 2014 *Int. Mater. Rev.* **59** 1
[43] Stannarius R 2017 *Rev. Sci. Instrum.* **88** 051806
[44] Müller C R, Holland D J, Sederman A J, D Mantle M, Gladden L F and Davidson J F 2008 *Powder Technol.* **183** 53–62
[45] Penn A, Boyce C M, Conzelmann N, Bezinge G, Pruessmann K P and Müller C R 2019 *Chem. Eng. Sci.* **198** 117–23

[46] Boyce C M, Penn A, Lehnert M, Pruessmann K P and Mueller C R 2019 *Chem. Eng. Sci.* **200** 147–66

[47] Grudzien K, Niedostatkiewicz M, Adrien J, Tejchman J and Maire E 2011 *Chem. Eng. Proc.: Process Intensification* **50** 59–67

[48] McDonald S A, Schneider L C R, Cocks A C F and Withers P J 2006 *Scr. Mater.* **54** 191

[49] McDonald S A, Schneider L C R, Cocks A C F and Withers P J 2012 *Int. J. Mater. Res.* **103** 162

[50] Chandler H W, Sands C M, Song J H, Withers P J and McDonald S A 2008 *Int. J. Solids Struct.* **45** 2056

[51] Hall S A, Bornert M, Desrues J, Pannier Y, Lenoir N, Viggiani G and Bésuelle P 2010 *Géotechnique* **60** 315

[52] García-Moreno F, Kamm P H, Neu T R, Bülk F, Mokso R, Schlepütz C M, Stampanoni M and Banhart J 2019 *Nat. Commun.* **10** 3762

[53] Takano H, Morikawa M, Konishi S, Azuma H, Shimomura S, Tsusaka Y, Nakano S, Kosaka N, Yamamoto K and Kagoshima Y 2017 *J. Phys.: Conf. Ser.* **463** 012025

[54] Maire E, Bourlot C L, Adrien J, Mortensen A and Mokso R 2016 *Int. J. Fract.* **200** 3

[55] Fischer F and Hampel U 2010 *Nucl. Eng. Des.* **240** 2254

[56] Hoppe D 2013 *TM-Tech. Mess.* **80** 261–71

[57] Hoppe D 2015 *TM-Tech. Mess.* **82** 317–22

[58] Brodu N, Dijksman J A and Behringer R P 2015 *Nat. Commun.* **6** 6361

[59] Bertrand T, Peixinho J, Mukhopadhyay S and MacMinn C W 2016 *Phys. Rev. Appl.* **6** 064010

[60] Dijksman J A, Zheng H and Behringer R P 2013 *AIP Conf. Proc.* **1542** 457–60

[61] Dijksman J A, Brodu N and Behringer R P 2017 *Rev. Sci. Instrum.* **88** 051807

[62] Barthel F, Bieberle M, Hoppe D, Banowski M and Hampel U 2015 *Flow Meas. Instrum.* **46** 196–203

[63] Bieberle M and Barthel F 2016 *Chem. Eng. J.* **285** 218–27

[64] Waktola S, Bieberle A, Barthel F, Bieberle M, Hampel U, Grudzien K and Babout L 2018 *Exp. Fluids* **59** 69